Chapter 6

Design Solutions

To understand the physics of an RF ion thruster discharge chamber, a numerical model is needed. Goebel develop an analytical 0 D-model using volume averaged to calculate the performance and efficiency but even though the model lacks spatial resolution. It manages to predict the performance of an RF thruster with good agreement. However, it does not consider the effect of one-dimensional field distribution. It does not describe the power transfer efficiency from the coil to the plasma and does not treat neutral gas heating. Therefore, the analytical model needs to be further improved and tested for evaluating the performance of smaller-size thrusters. To overcome this problem, Charbert [48] reported that the analytical model could be improved by considering power transfer efficiency. The goal of this study is to develop a global model of a gridded ion thruster by using Iodine as a propellant and powered by a radio frequency inductive coil. In the early stage of this model, it required accurately measuring plasma parameters to predict thruster performance. Later it was improved by taking self-consistent calculations of the neutral pressure, electron temperature and recycling charged particle in thruster volume. These parameters quantify the thruster properties (thrust, specific impulse, thrust efficiency, mass-utilization, and power transfer efficiency) can be found. By improving Goebel's analytical model some modified physical phenomena such as non-constant ion-confinement effect caused by the magnetic field, non-constant Clausing factor, secondary electron emission, and doubly ionized ions are also considered.

6.1 Discharge Chamber

Compared with different Electric Propulsion technologies, Radio Frequency Ion Thrusters (RIT) has the simplest configuration [45] . With this configuration, RIT has characteristics of low power requirement, longer lifetime, and high specific impulse. An RF coil is wrapped around an insulating chamber with a gas feed system. The most important component of RIT is the geometry of the discharge chamber, which signifies the performance of the thruster.

6.2 Effective Length of Discharge Chamber

The shape of the discharge chamber could be hemispherical, cylindrical, or conical shaped connected to an ion accelerator assembly. The significance of discharge chamber diameter with varying thrust range for RIT has been verified by the researchers at Giessen University [Wahlter et al 175]. The length of the discharge chamber affects the ionization of the neutral particles. For analyzing the length of the discharge chamber through calculations, an experiment has been carried out and an

empirical relation is summarized by [Loeb et al. 2004].

$$L_{opt} = (R)^{.66} + d \tag{6.1}$$

where: L_{opt} is the optimized length of the discharge chamber, d is the length of gas distributor introduced into DC and R is the radius of DC. In this experiment, a diameter of 50 mm (RIT) with different discharge lengths 27.6 mm, 30 mm, 31.9 mm, 35.5 mm, 40 mm, recorded with different performances under similar conditions. Applying the same RF power and mass flow rate, RF thrusters with 50 mm diameter have the optimal performance in beam current and efficiency with the discharge length of 30 mm [50]. The optimal ratio of length to the diameter of DC by adjusting ionization length, thruster had the minimum discharge cost and maximum propellant utilization efficiency [Kong et al. 2018].

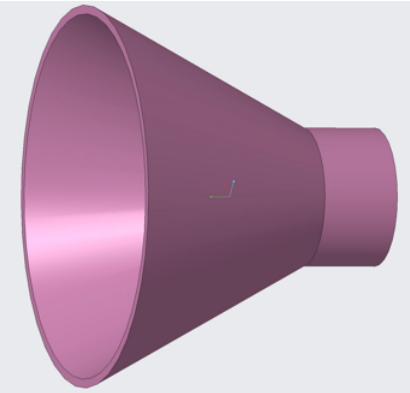

Figure 6.1: CAD model of the discharge chamber.

6.3 Ionization

RF ionization technique is quite difficult to perform with RF propagating waves is challenging as well. RF waves produce an electric field in an azimuthal direction. For this, a driving frequency must be carefully selected and to prevent power loss in the coil. It is necessary to be selected a valid design of an impedance matching network with the number of coils to maximize efficiency [45]. There are three main parts for RF ionization - RF power supply, Antenna element, and matching network.

6.3.1 RF Generator

A high-frequency discharge chamber coupled with inductive coils is utilized as an ion generator with applying an RF current in these coils provided by a radio frequency generator (RFG) with suitable frequency. An electromagnetic field is applied inside the discharge chamber. Thus, in a closed-loop path, free electrons are accelerated and can ionize injected propellant gas by electron impact ionization. The frequency range is 1.36 MHz to 13.6 MHz. But the typical frequency range is 1.56 MHz, which is the best option for ionization, and the field penetration from the coil at the boundary is limited by the depth in the plasma [51]. RF ionization system depends on a Power Processing Unit (PPU). The PPU contains an RF generator and provides a suitable frequency and power level.

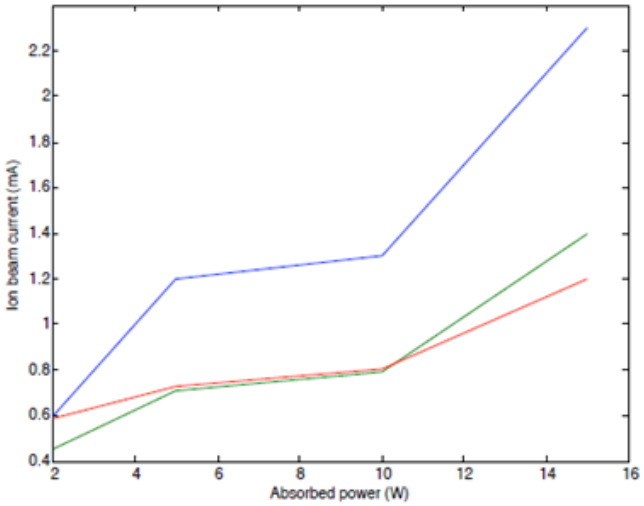

Figure 6.2: Ion beam current as a function of absorbed power for three different frequencies. The blue line represents 1.56 MHz, the green line 8 MHz, and the red line 13.56 MHz [51].

6.3.2 Antenna Element

The antenna in RF thrusters is made of a conductive material (commonly copper), which is mounted on insulating material walls made of such as quartz or alumina for inductive discharge. RF supply load is on the antenna element (coils) that are winded on the discharge chamber body. Which are used to induce a magnetic field inside the chamber is given by.[52]

$$B = \mu_0 N I \tag{6.2}$$

where: N is the number of winding turns per meter, I is the current in the coil and μ_0 is the permeability of free space. The induced magnetic field by the RF coils depends on coil wire size and the amount of power supply. A maximum of 9.77 turns per centimeter or coil occupies 1 turn/centimeter and the impedance of the coil is 50 Ω [52]. For an input power of 500 W and this would give in 10 A of RF current in the coils. For this data, a magnetic field of 12.6 G (a low field strength) is induced [52]. The electron Larmor radius for an electron temperature of 5 eV is about 6 mm, so electrons are magnetized in the radial direction. This field of strength is sufficient to affect the radial electron motion, which reduces the ion loss to the discharge chamber loss. Assuming a

Figure 6.3: CAD model of the RF antenna [52]

3 AWG copper wire (diam = 5.83 mm) with a maximum 5 number of turns. If we increase the number of turns then it decreases the number of collisions in the plasma sheath and degrades the

efficiency of the thruster. The plasma sheath thickness is directly proportional to the cube of the number of turns insulated [52].

6.3.3 Matching Network

During the ionization process, discharge is driven by a power source but if we have an impedance mismatch power is not transferred efficiently from source to discharge. Therefore, a matching network between source and ionization coil is required to maximize power transfer. A matching network is installed before the RF energy can be transferred into the antenna element [53]. Each

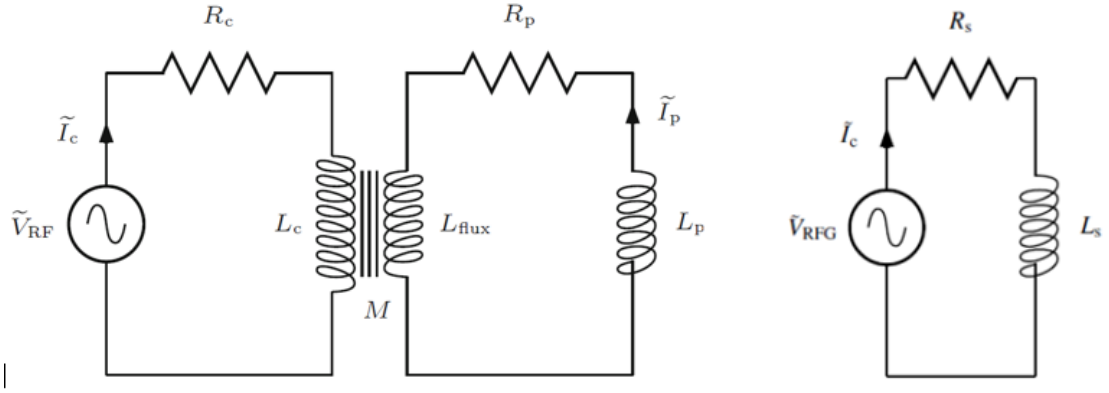

Figure 6.4: Equivalent circuit of an inductive plasma discharge (a). Effective load seen by the RFG (b).[54]

conductor used has its own characteristics impedance value. For maximum power transfer between the RF source and the load, output impedance must be equal to the load impedance [53]. The

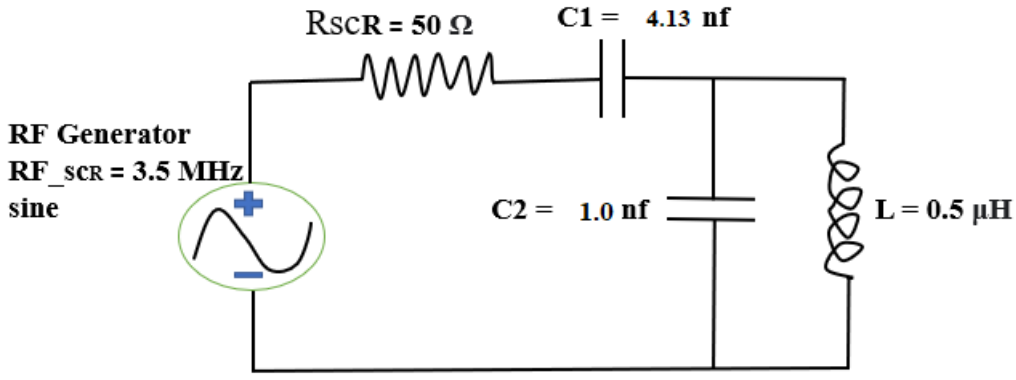

Figure 6.5: Equivalent circuit representing the antenna L, the RF generator and its internal impedance, and the matching network consisting of C1 and C2.

design parameters for the matching network. Calculations and theory regarding this design are given in appendix A.

These two impedances must be equal otherwise the coil will start reflecting the power back into the PPU, which cause power loss.

6.4 Propellant Gas – Iodine

Table 6.1: Propellant Gas properties[55]

Elements	I_2	I	X_e
Mass [amu]	253.81	126.90,	131.29
First Ionization Energy (IE1-eV),	9.3	10.5	12.1
Storage Density (g/cm^3) @15^0C, 1.013 bar,	4.9	...	5.5 x 10^-3
Cost (ϵ/kg),	480	...	3600

As we can observe the ionization energy of atomic and diatomic iodine is lower than X_e so, it would give a higher electron density in iodine plasma. Iodine is diatomic, it has additional energy loss channels (dissociation). Also, the initial pressure P_0 is higher for X_e compared to Iodine for the same neutral gas flow rate. Iodine plasma contains more I^+ and I_{2^+} with a density five times higher at the child-Langmuir limit which is explained by the high dissociation rate of diatomic iodine. Doubly ionized I^{++} ions are neglected because of a large gap between first and second ionization potentials.

Mass flow rate In this model, gas heating and gas depletion phenomenon are neglected, and neutral gas assumed to be ideal, uniform with constant density n_g and temperature T_g. The pressure in the discharge chamber in $[mT_{orr}]$ is provided as an input parameter [55]:

$$n_g = 0.133 * \frac{P[mT_{orr}]}{k_B T_g} \tag{6.3}$$

At steady state, when plasma is switched off, then neutral gas flow rate is defined by:

$$Q_0 = \frac{1}{4} n_{g0} v_{g0} A_g \tag{6.4}$$

where: n_{g_0}-neutral gas density and v_{g0}-mean speed with plasma Assume there is no dissociation in I_2 in initial state so:

$$P_0 = n_{g0} K_B T_{g0} \tag{6.5}$$

We obtain initial pressure in the discharge chamber:

$$P_0 = \frac{4 K_B T_{g0} Q_0}{v_{g0} A_g} \tag{6.6}$$

When plasma is on, electron-neutral collision processes produce both I^+ and I_2^+ which are accelerated across the screen and accelerated grids with an applied potential difference V_{grid}. This leads to a velocity of expelled existing beam of ions:

$$v_{Beam} = \sqrt{\frac{2eV_{grid}}{M_x}} \tag{6.7}$$

Physical Parameters

Table 6.2: Physical Parameters

Discharge Size in O_x direction	l_x	30	mm
Discharge size in O_y direction	l_y	50	mm
Neutral gas pressure	P_n	0.1-100	mTorr
Neutral gas density	n_g	$0.42 * 10^{18} - 6 * 10^{18}$	m^{-3}
Mass flow rate	Q_0	0.20 – 5.944mg/s (2 sccm – 30 sccm)	mg/s
Ion mean free path	λ_i	4.64	cm
Neutral gas temperature	T_g	$300^0 k$	k
Excitation frequency	f_{RF}	3.5	MHz

6.5 Global Model of Plasma [57,58]

6.5.1 Power transfer in Pure - Inductive Discharge

Plasma generation is done by passing a circulating RF current (I_{coil}) with an amplitude of frequency, which passes through a coil located around the thruster body. This induces an electron magnetic field inside the chamber and breakdown the gas for plasma generation. For inductive heating, power transfer by RF generator with a matching network is the sum of power dissipated in the coil and power absorbed by the plasma [55],

$$P_{RF} = P_{coil} + P_{abs} \tag{6.8}$$

$$P_{coil} = \frac{1}{2} R_{coil} (\frac{I_{coil}^2}{V}) \tag{6.9}$$

$$P_{abs} = \frac{1}{2} R_{ind} (\frac{I_{coil}^2}{V}) \tag{6.10}$$

R_{coil} = Coil resistance R_{ind} = Effective inductive resistance

Finally, Electron energy density is given by the global electron power balance:

$$\frac{d}{dt}(\frac{3}{2} e n_e T_e) = P_{abs} - P_{loss} \tag{6.11}$$

Power Balance-RF Generator

$$P_{RF} = P_{coil} + P_{abs} \tag{6.12}$$

$$P_{RF} = \frac{1}{2}(R_{ind} + R_{coil})(\frac{I_{coil}^2}{V})) \tag{6.13}$$

$$P_{abs} = \frac{1}{2} R_{ind} (\frac{I_{coil}^2}{V}) \tag{6.14}$$

where: $R_{ind} = N^2 \ R_p$

$$P_{abs} = \frac{1}{2} N^2 R_p (\frac{I_{coil}^2}{V}) \tag{6.15}$$

Plasma Resistance - R_p

$$R_p = \frac{\pi R}{\sigma_{eff} l \delta_P} \tag{6.16}$$

where: δ_{eff} **collision less skin depth**

$$\delta_P = (\frac{m}{e^2 \mu_0 \eta_s})^{\frac{1}{2}} \tag{6.17}$$

here, the n_s is the plasma density at the sheath edge which is around 40% lower than the plasma density at the center.

$$n_s = 0.60 * n_0 \tag{6.18}$$

where: σ_{eff} **effective conductivity**

$$\sigma_{eff} = \frac{e^2 \eta_s}{m_e \nu_{eff}} \tag{6.19}$$

where: ν_{eff} **effective collision frequency**

$$\nu_{eff} = \nu_{ei} + \nu_{stoc} + \nu_{en} \tag{6.20}$$

(i).The electron-ion collision frequency is:

$$\nu_{ei} = 2.91 * 10^{-}12 \frac{\eta_i ln\wedge}{T_e^{\frac{3}{2}}} \tag{6.21}$$

$$ln\wedge = 23 - 0.5 * ln(\frac{10^{-6} * m^3.n_0}{V^{-3}.T_e^3}) \tag{6.22}$$

Note: In low pressure discharge the value of electron-ion collision frequency ν_{ei} can be omitted.

(ii). Collisionless stochastic heating is regarded as the dominant heating mechanism at lower discharge pressures where in terms of $\nu_m < \omega$. The stochastic collision frequency calculates to:

$$\nu_{stoc} = \frac{\overline{v}_e}{4 * \delta_{stoc}} \tag{6.23}$$

with anomalous skin layer depth:

$$\delta_{stoc} = (\frac{c^2 \overline{v}_e}{\omega \omega_{pe}})^{\frac{1}{3}} \tag{6.24}$$

$\bar{v_e}$ is the thermal electron velocity given as:

$$\bar{v_e} = \sqrt{\frac{8kBT_e}{\pi m_e}} \tag{6.25}$$

where: ω_{pe} is electron plasma frequency is given by:

$$\omega_{pe} = \sqrt{\frac{n_0 e^2}{m_e \epsilon_0}} \tag{6.26}$$

High density, $\delta << R, l$ and low pressure regime $\nu_m < \omega$ where:

$$\delta = \frac{c}{\omega_{pe}} \tag{6.27}$$

(iii). ν_{en} is the electron-neutral frequency:

$$\nu_{en} = \sigma\sqrt{\frac{8kBT_e}{\pi m_e}} \tag{6.28}$$

$$\sigma = 6.6 * 10^{-}19[\frac{T_e}{4} - 0.1/(1 + \frac{T_e}{4})^{1.6}] \tag{6.29}$$

Correction: estimations of R_{pl} valued obtained for different inert gasses are close of elastic collision does not exceed $3 * 10^7\ sec^{-1}$. This fact confirms the collisional nature of RF power absorption [59].

- **Plasma Parameters - Electron temperature range (1 eV - 6 eV)**

Table 6.3: Calculated Plasma Parameters

Collision skin depth	δ	0.0168 m
Collision less skin depth	$\delta_e ff$	(0.0205 - 0.0276) m
Collision skin depth	δ_p	0.0217 m
Effective conductivity	$\sigma_e ff$	(44.22 - 37.65) mho/m
Electron-ion Colli freq	ν_{ei}	–
Stochastic colli freq	ν_{stoc}	$(8.13 * 10^6 - 1.47 * 10^7)$
Electron-neutrals Colli freq	ν_m	$3 * 10^7$
Effective Collision freq	$n_{eff} = \nu_{ei} + \nu_{stoc} + \nu_m$	$(3.81 * 10^7 - 4.49 * 10^7)$
Thermal electron velocity	$\bar{v_e}$	$(6.6 * 10^5 - 1.63 * 10^6)$
Excitation frequency	f_{RF}	3.5 MHz
Plasma freq	ω_{pe}	$1.78 * 10^10$
Applied angular freq	ω	$2.2 * 10^7$
Const atomic Ioniz cross-section frac	σ_0	$2.3 * 10^8$
Plasma Resistance	R_p	(1.85 - 2.176) Ω
Power abs by the plasma	P_{abs}	$(10 - 147.5)\ kW/m^3$
Power supplied to RFG	P_{RF}	$9.784 - 143.80\ Watts$

6.5.2 Particle Balance Equations

These are written for each species of time variation densities described as the net result of the production and destruction of electrons, positive and negative ions and neutrals. The relevant particle loss areas to the thruster walls/grids used in the balance equations from [55] :

$$A_{wall1} = \pi * l * (r_1 + r_2) \tag{6.30}$$

$$A_{wall2} = \pi * (r_1^2 + r_2^2) \tag{6.31}$$

are the areas of the radial and back walls.

- $A_i = A_{wall2}.\beta_i$ and $A_g = A_{wall2}.A_g$ are the effective open areas of the grids over which ions and neutrals escape the thruster.

- A_{grid_i} = A_{wall2} - A_i and A_{grid_n} = A_{wall2} - A_g are the effective loss areas of the grids for ions and neutrals.

- $A_{eff_i} = A_{wall1}\ h_R + 2{*}A_{wall2}{*}h_L = \pi{*}(r_1^2 + r_2^2){*}h_L + \pi{*}l{*}(r_1 + r_2){*}h_R$ is the total effective area for positive ion and electron wall losses, where edge to center plasma density ratios h_L and h_R used to define for plasma density profile in the thruster. At low to intermediate gas pressures, the wall losses are very important to determine both the electron temperature and the density of the various species. Therefore, both the parameters h_L and h_R strongly depend on the neutral gas pressure P and n_0.

$$h_L = 0.86[3 + \frac{l(n_{I_2} + n_I)\sigma_i}{2}]^{-\frac{1}{2}} = 0.86[3 + \frac{l * n_g * \sigma_i}{2}]^{-\frac{1}{2}} = 0.86[3 + \frac{l}{2\lambda_i}]^{-\frac{1}{2}} \tag{6.32}$$

$$h_R = 0.80[4 + R(n_{I_2} + n_I)\sigma_i]^{-\frac{1}{2}} = 0.80[4 + R * n_g * \sigma_i]^{-\frac{1}{2}} = 0.80[4 + \frac{R}{\lambda_i}]^{-\frac{1}{2}} \tag{6.33}$$

where: $(n_{I_2} + n_I) = n_g$, The equation h_L center to edge ratio is used for electropositive plasma, which is justifies for low electronegative plasmas has been developed and ion neutral mean free path $\lambda_i = \frac{1}{n_n \sigma_{in}}$ with neutral gas density n_n and ion-neutral momentum transfer cross-section σ_{in}.

- $A_{eff_P} = A_{wall1}{*}h_L + A_{wall2}{*}h_R + A_{grid_i}{*}h_L$ is the area for positive ion wall neutralisation ($A_{eff_i} = A_{eff_P} + A_i$) the ions lost are either accelerated by the grids or neutralized to produce neutrals.

- $A_n = A_{wall1} + A_{wall2} + A_{grid_n}$ is the area for iodine neutral atom wall losses and production of I_2 by wall recombination.

Table - Particle balance and Plasma confinement parameters

Table 6.4: Particle loss areas to thruster walls/grids

Wall-1	A_{wall_1}	0.0032 m^2
Wall-2	A_{wall_2}	0.0022 m^2
Effective open area of the grids	A_i	0.00155 m^2
Effective loss areas of the grids	A_{grid_i}	6.65 x 10^{-4} m^2
Total effective area for wall losses	A_{eff_i}	0.0023 m^2
Area for positive ion wall neutralisation	A_{eff_P}	7.039 x 10^{-4} m^2
Area for iodine neutral atom wall losses and production	A_n	0.0069 m^2
Plasma density profile-Axial sheath density	h_L	0.129
Plasma density profile-Radial sheath density	h_R	0.092
Effective plasma size	d_{eff}	0.052 m
Electron density	n_e	$(4.7{*}10^{17} - 5.9{*}10^{18})\ m^{-3}$
Power loss in the plasma	P_{RF}	$(9.78 - 143.80)\ Watts$

6.5.3 Plasma Confinement [57,58]

The plasma ions are produced by ionization of neutrals, at a rate k_{iz}

$$k_{iz} = 2.34 * 10^{-14} * T_e^{0.59} * e^{-}(\frac{17.44}{T_e}) \tag{6.34}$$

Assuming nearly uniform plasma in conical shape and Maxwellian electrons absorbing electrical power P_{abs}. We can determine the electron temperature T_e of the plasma by equating the total surface particle loss to the volume ionization:

$$n_0 u_B[2\pi(r_1^2 + r_2^2) + 2\pi l'(r_1 + r_2)] = k_{iz} n_g n_0 \pi V \tag{6.35}$$

where: $l' = \sqrt{(r_1 - r_2)^2 + r_1 * r_2}$, lateral length of the discharge chamber $V = \frac{\pi}{3} l(r_1^2 + r_2^2 + r_1 * r_2)$ volume of the discharge chamber.

For equality equation we can describe as:

$$\frac{k_{iz}(T_e)}{u_B(T_e)} = \frac{1}{n_g * d_{eff}} = \frac{5 \times 10^{-14} e^{-(\frac{-15.7}{T_e})}}{\sqrt{\frac{KT_e}{m_i}}} \tag{6.36}$$

where: $u_B = \sqrt{\frac{k_B T_e}{m_i}}$ Bohm velocity. The effective plasma size for particle loss within conical discharge chamber calculates:

$$d_{eff} = \frac{1}{2} \frac{Rl}{Rh_L + lh_R} \tag{6.37}$$

where: l denotes the discharge chamber axial length and R is the effective radius, respectively. h_l is the pressure dependent ratio of the ion density at the top sheath edge to the ion density at the center of the plasma. h_R is the ratio of ion density at radial sheath edge to the center described by [Godayk et.al].

6.5.4 The Low-Pressure, High frequency limit at a high density

It is already defined $[Ch_7 IDischarge]$ that in high density regime the skin depth is small and and the resistance of the inductive branch is $R_ind = N^2\ R_P$. So the power balance is [57,58]:

$$P_{loss} = P_{abs} = \frac{1}{2} R_{ind} I_{coil}^2 = \frac{1}{2} N^2 R_P I_{coil}^2 = 2 n_e u_B (A_1 h_l + A_2 h_R) \epsilon_T(T_e) \tag{6.38}$$

By using this expression of R_P we can define the electron density as a function of the coil current in the inductive mode:

$$n_e = [\frac{\pi R N^2 \nu_m (\frac{m}{\epsilon_0}^{\frac{1}{2}})}{4 u_B (A_1 h_l + A_2 h_R) e \epsilon_T(T_e).l.c}]^{\frac{2}{3}} * (I_{coil})^{\frac{4}{3}} \tag{6.39}$$

This gives that the fixed current the electron density increases with the number of turns and with the gas pressure. Therefore, ν_m increases linearly with the gas pressure while h_l and h_R decrease with the gas pressure.

6.5.5 Energy lost in the volume - Lieberman and Lichtenberg [57]

Energy Loss from the plasma by Maxwellian electrons

$$\epsilon_e = 2 * Te + Vs \tag{6.40}$$

with V_s is the sheath voltage is given by:

$$V_s = Te * ln(\frac{mi}{2 * pi * me}) \tag{6.41}$$

Ion kinetic energy loss at the surface

$$\epsilon_i = \frac{Te}{2} + Vs \tag{6.42}$$

Energy Loss per Electron–Ion Pair Created A very important quantity that we use to calculate is the collisional energy loss per electron–ion pair created, $\epsilon_c(Te)$, which is defined as:

$$k_{iz}.\epsilon_c = k_{iz}.\epsilon_{iz} + k_{ex}.\epsilon_{ex} + k_{el}.\epsilon_{el} \tag{6.43}$$

$$k_{iz}.\epsilon_c = k_{iz}.\epsilon_{iz} + k_{ex}.\epsilon_{ex} + k_{el}.(3\frac{m_e}{m_i}.Te) \tag{6.44}$$

The quantity $\frac{3*me}{mi} * Te$ is the mean energy lost per electron for a polarization scattering. Summing the three contributions yields the total energy lost per electron–ion pair from the system:

$$\epsilon_T = \epsilon_e + \epsilon_i + \epsilon_c \tag{6.45}$$

Reaction rates

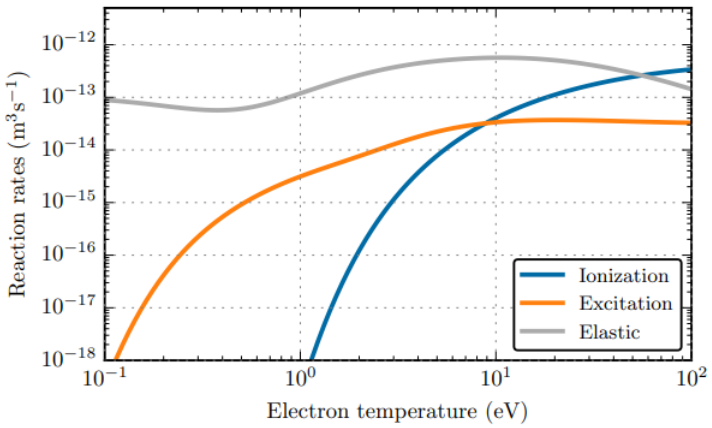

Figure 6.6: (a) Reaction rates for the iodine I atom as a function of electron temperature.[Principal of Plasma].

Threshold energies of the reaction used in the model, found as the energy corresponding to the first non-zero cross-section (left), and the other admitted value from the literature (right),

- **Table:Total energy loss per electron-ion pair with electron temperature (1 eV - 6 eV)**

Energy	Used in this work	Other admitted value
$\mathcal{E}_{diss.iz}$	10.9 eV [33]	
$\mathcal{E}_{iz,I_2}$	9.31 eV [33]	
$\mathcal{E}_{diss,I_2}$	1.567 eV [33]	1.529 eV [72]
$\mathcal{E}_{exc,I}$	0.95 eV [33]	0.94 eV [70]
$\mathcal{E}_{iz,I}$	11.6 eV [33]	10.45 eV [34]
$\mathcal{E}_{detach}$	4 eV [65]	3.059 eV [71]
$\mathcal{E}_{diss,I_2^+}$	2.1768 eV [65]	

Table 6.5: Total energy loss per electron-ion pair with electron temperature (1 eV - 6 eV)

ϵ_c	$\epsilon_{iz} + \frac{k_{ex}}{k_{iz}}.\epsilon_{ex} + \frac{k_{el}}{k_{iz}}.\epsilon_{el}$	$(15.047 - 90.28)\ Volts$
ϵ_e	$2 * Te + \mathrm{Vs}$	$(5.13 - 30.80)\ Volts$
ϵ_i	$\frac{Te}{2} + \mathrm{Vs}$	$(4.073 - 24.44)\ Volts$
ϵ_T	$\epsilon_e + \epsilon_i + \epsilon_c$	$(24.25 - 145.53)\ Volts$

6.6 Ion optics

The most important component of ion thruster is Ion optics. Once the plasma is generated in the discharge chamber, ions must be extracted and accelerated by a grid assembly. So, in these grid configurations (thickness, aperture size of the screen, accelerator, and decelerator grid), the best material options and manufacturing process are analyzed. This work shows an extensive literature review, information about ion optics compared with significant ion thrusters. There are some important decisions to calculate the ion optics parameters that have already been taken:

- The shape of the grids shall be circular and 5 cm in diameter to fit with the discharge chamber.
- These grids will contain circular apertures and hexagonal packed.
- The screen grid aperture diameter is designed close to its maximum value desirable to minimize the transparency of acceleration grid to limit neutral flow.
- Screen grid is directly exposed to chamber plasma and designed to be as thin as possible to increase transparency.
- The reduction in gap (closer the grids) at operating temperatures increases the perveance value.
- There shall be a spacer between the grids to insulate them from each other.

In the development of a complete design for ion optics, the following parameters must be determined:

- Number of Grids
- Spacing between the grids
- Grid's thickness and grid transparency
- Screen grid aperture diameter

- Acceleration grid aperture diameter
- Aperture pattern
- Thermal Expansion of Grids
- Construction Materials
- Insulating Spacing material between the Grids
- Voltage across each grid
- The beam currents.

6.7 Grid Configurations and main parameters

6.7.1 Independent Variables

There are six unknown variables: screen grid thickness ts, screen grid hole diameter d_s, grid spacing lg, accel grid thickness ta, accel grid hole diameter d_a, and accel grid voltage Va.

- **Number of Grids**

As already mentioned in subsection 2.3.1 the grid configuration consists of three grids assembly in ion thruster. These grids are set at different potentials to extract and optimally focus the ion beam. Screen grid relates to a higher potential, accelerator grid is connected with negative potential. While stopping electron backstreaming decelerator grid-connected with zero potential.

- **Spacing between the grids and maximum applied electric field**

The distance between the screen and acceleration grids is chosen to be is 0.6 mm after studying various research materials with similar sizes of scaling of thrusters like the Miniature Microwave Ion Thruster (MMIT) [61]. Increasing the thrust density between this section requires a reduction of hot gap distance d. The maximum electric field applied to the grids as a function of grid spacing for CC materials is shown in the figure. By using the curve fit equation, obtains a maximum electric

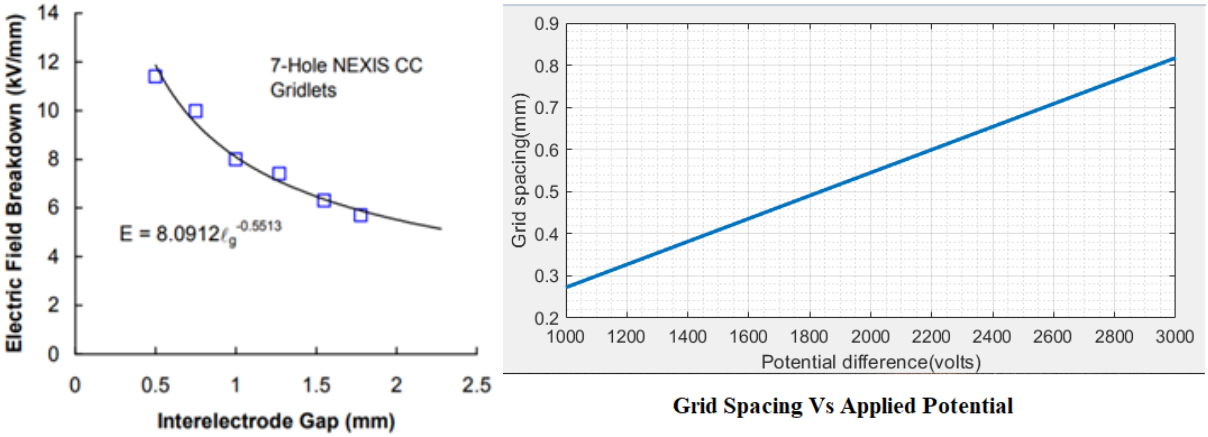

Figure 6.7: (a). Grid Set 1: Maximum electric field for partially to fully conditioned CC Gridlets at various grid gaps [62] (b). Grid Spacing vs potential difference

field of 11.85 kV/mm for a grid-gap of 0.5 mm (4% higher than measured and 5 kV/mm (through

extrapolation to 2.36 mm spacing) for NEXIS nominal grid spacing. It should be noted that using the enhanced electric field of 5400 kV/mm for CC one obtains a predicted maximum electric field of 4.5 kV/mm (+/- 10%) for the NEXIS nominal grid-gap [53,62].

Carbon-Carbon Composite material $E = 11kV/mm$ = (1.0 mm distance) $E = 5.5kV/mm$ = (0.5 mm distance) with 50% margin should be considered: then $E = 3.67kV/mm$

- **Aperture Pattern**

Grid apertures are typically circular and packed in a hexagonal array. The hexagonal pattern ensures that the distance between each pair of grid apertures is minimized. This offers two main advantages. First, the number of apertures is maximized allowing larger ion density to pass through. Second, the solid area (grid wall) between each pair of apertures is minimized which reduces the probability of ion impingement and minimizes sputtering of material while maintaining the structural integrity of the grids. As it can be seen the length of the grid wall between every two apertures is chosen to be 0.2 mm. this is determined firstly by the manufacturing limitation and secondly by the hardness of the material used [53,62,63].

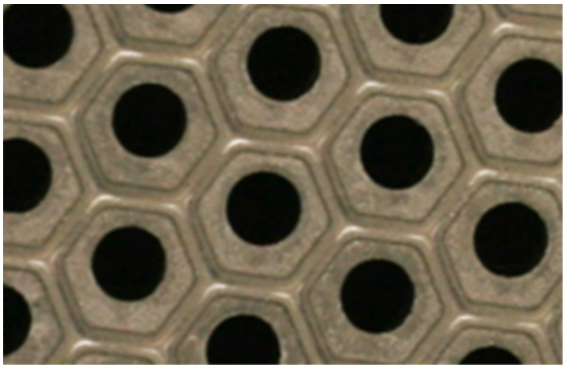

Figure 6.8: Grid apertures typically circular and packed in a hexagonal array.

- **Aperture diameter calculation**

Ion optics apertures are typically circular and hexagonal packed array to produce high transparency for ions in plasma sources. It is necessary to reduce the dimensions of an aperture at plasma boundary in order of Child-Langmuir distance to establish the sheath that will accelerate the ions to high energy with good focusing and reflect the electrons from the plasma [1,53]. At this point, we can calculate the acceleration grid aperture diameter. By solving for D, the aperture diameter is 1.9 mm was calculated by using equation [53]:

$$D = \sqrt{\frac{9I_b L^2 \sqrt{M_I}}{\pi \epsilon_0 \sqrt{2} e V_T^{\frac{3}{2}}}} \tag{6.46}$$

The screen grid aperture diameter should be greater than the acceleration grid aperture diameter to produce good focusing and maximize the number of apertures. For higher propellant efficiency, the screen grid should be capable of keeping as many neutral propellant atoms as possible inside the chamber as well [53]. Due to lack of resources and time for doing such testing, it was discussed and proposed that the screen grid aperture diameter should be 20 % greater than the accel grid aperture. This proposal relies both on calculations of effective area utilization, and consideration of the factors explained above [53]. This results in a diameter of 1.60 mm x 120 % = 1.90 mm.

- **Number of Aperture calculation**

The number of grid apertures is calculating by dividing the grid open area to the area per aperture [1]:

$$N_{aperture} = \frac{f_a \pi r_{grid}^2}{\pi r_{aperture}^2} = \frac{f_a r_{grid}^2}{r_{aperture}^2} \tag{6.47}$$

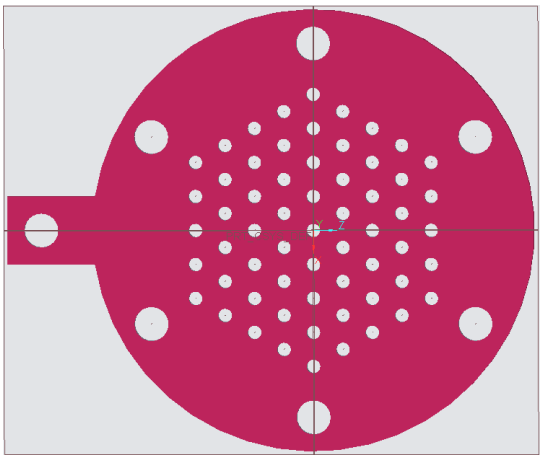

Figure 6.9: Grid with apertures in a hexagonal pattern.

Diving the grid diameter by screen grid aperture diameter, the number of apertures to fit on one row of the grid is known. The calculated result is 326 and the same space between each aperture must be in place.

So combined with the hexagonal requirement of having an odd number of apertures along the middle, the choice fell on using 326 apertures.

The maximum aperture current is obtained by using the definition of the beam flatness, which is given by:

$$f_b = \frac{Averagecurrentdensity}{Peakcurrentdensity} = \frac{\overline{I}_{aperture}}{I_{aperture}^{max}} \tag{6.48}$$

The published value of NSTAR beam flatness is 0.47 $[Polk_{30}]$. $f_a = 0.34$ and $f_s = 0.47$

- **Grid thickness and grid transparency**

The thickness of the size of the grid should be ts = 0.39 mm and ta = 0.51 mm based on ion engine testing with similar dimensions in the past [62]. The grids should provide satisfactory transparency, while on another side, these have sufficient robustness to service vibrations during launch. The grids also must have such thickness that erosion does not affect their life to a big extent.

Table 6.6: Ion Optics

Grid part	Material	Aperture Diameter (mm)	Thickness (mm)
Screen Grid,	CC	1.90	0.39
Accel Grid,	CC	1.60	0.51
Spacer	MACOR	–	0.50
Number of Apertures	N_h	–	326

- **Thermal Expansion of Grids (CEX2D and CEX3D both**

To reduce the erosion of the accelerator grid which is caused by backstreaming and Charge Exchange (CEX) ion collisions, two grid system is added with a decelerator grid at a lower potential to block reflux CEX ions. A decelerator grid can effectively reduce pit and groove erosion [72]. More recently, 2-D and 3-D grid erosion models CEX2D and CEX3D were developed at JPL to help understand these erosion mechanisms [64], [65]. In a three-grid system, most of the charge-exchange ions created downstream of the grid plane will impact the decel grid at relatively low energies ($\backsim 0 - 25V$), instead of impacting the accel grid at high energies ($\backsim 200V$), thus it is reducing overall erosion (Chapter-5)[1].

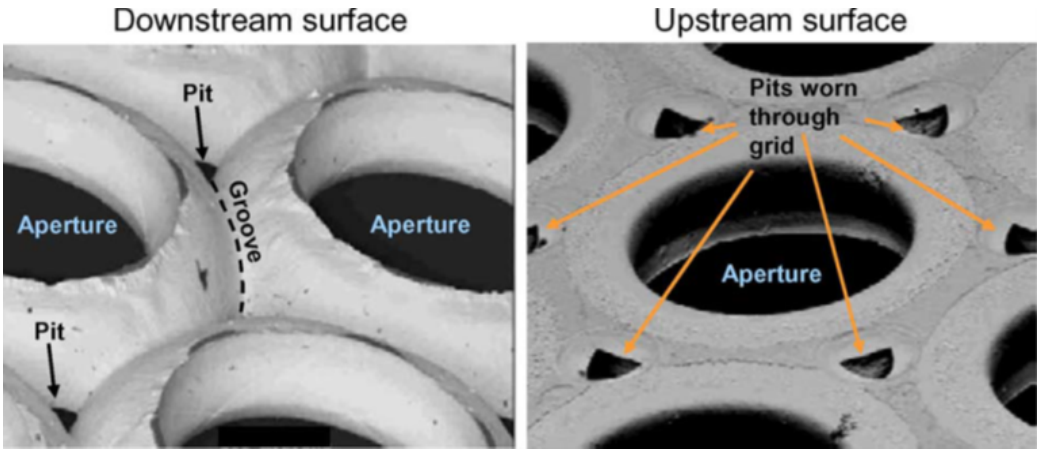

Figure 6.10: SEM images of the NSTAR accel grid after 30352 h of operation.

The accel grid experienced significant erosion on the downstream surface in a "pits and grooves" pattern. In the center region of the grids, the "pits" were worn through the grid around many of the apertures. Grid apertures were widened by $\backsim$ 25% while minimal erosion occurred on the upstream surface [66] array.

- **Grid Construction Materials**

The grids are manufactured CC-composite, Pyrolytic graphite, molybdenum, and Poco Graphite sheet by using laser micromachining due to a large number of apertures. Poco Graphite and molybdenum were found to sustain the highest electric fields while carbon-carbon composite and pyrolytic graphite displayed the lowest electric field values at the breakdown. Mo has a relatively high density, resulting in higher stress under dynamic loads. The high elastic modulus results in good rigidity, but this also increases stress under shock loads. Ti offers a 56% mass reduction over Mo while retaining good mechanical properties. PG, compared to Mo, has an order of magnitude lower strength and

stiffness, but it is much more resistant than graphite. CC presents mechanical properties like metals but with a much lower density which, combined with its near-zero CTE and low sputtering, makes it a very good option for ion engine grids [67]. Each grid is manufactured out of carbon-carbon (C-C) to achieve the best possible thermal stability.

- **Insulating Spacing material between the Grids**

Due to the high potential difference present between the grids, the best quality insulation must be provided between the screen grid, accelerator grid, and other components that have contact with the grid assembly. MACOR ring will be placed between the grids and function as a spacer to separate grids with compared to correct distance [68]. MACOR has low thermal conductivity and excellent electrical properties. It has excellent machinability compared to other Ceramics. Combined with great mechanical and thermal properties this is the best-suited material for spacers.

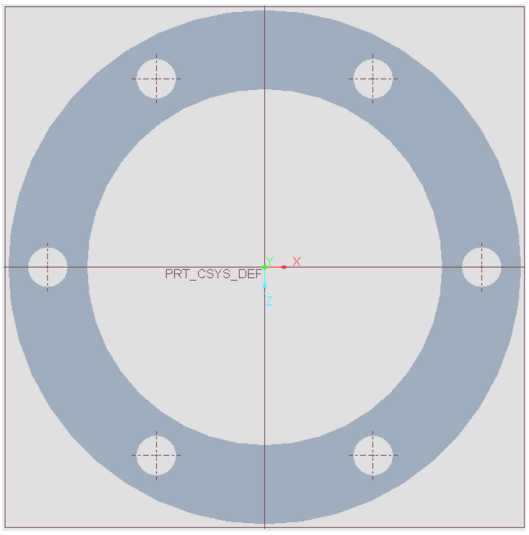

Figure 6.11: Insulating Spacing plate between the Grids

- **Voltage across each grid and the Beam Current**

When ions are inside the two grid regions they are accelerated. The final velocity is defined by V_N (net voltage) which is the difference between plasma and neutralizer potentials. The total voltage V_T is the difference between plasma and accelerator grid potentials applied across acceleration gap is acceleration voltage, which is defined as:

$$V_T = V_{sc} + |V_{accel}| \tag{6.49}$$

Here, V_{screen} and V_{accel} are the voltages at screen and acceleration. When computing the extraction capacity of the system it can be defined by the ratio of:

$$R = \frac{V_N}{V_T} = \frac{V_N}{V_{sc} + |V_a|} \tag{6.50}$$

For maximum extraction capacity at a point when $R = 0.8 \backsim 0.9$, which give higher values of current. In this case, we have $d = 0.60$ mm, $ta = 0.51, ts = 0.39$ mm, $Ds = 1.90$ mm, $Da = 1.60$ mm, and a total of 326 holes. For $R = \frac{V_N}{V_T} = 0.88$, $V_N = 1100$ V. Total exit potential = 1250-volt, Screen grid = 1100 volt, Acceleration grid = -150, but the total exit potential range is taken is (1000 - 1500) Volts.

The reported beam current in this case is I_B = (0.392 - 0.7218) A

6.7.2 This section contains an overview of the parameters elaborated in the above section:

Table 6.7: Ion optics parameters

Grid Parametres	
Beam Current	540 mA
Maximum Power Available	150 Wh
Acceleration Grid Voltage	150 volts
Screen Grid Voltage	1100 volts
Deceleration Voltage	25 volts
Diameter of the Grids	
Diameter of Accel Grid Apertures	1.60 mm
Diameter of Screen Grid Apertures	1.90 mm
Accel Grid thickness	0.51 mm
Screen Grid thickness	0.39 mm
Space between Grids	0.60 mm
Grid Material	CC
Insulation Spacer Material	Macor
Number of Apertures	326

The Clausing factor is used to describe the conductance reduction due to finite grid thickness which is 0.50 [85] for ion thruster that could be calculated with Monte Carlo gas code. The particles with randomized velocities that are injected into the start end of the discharge chamber further move into the ion optics are simulated by Monte Carlo code. The Monte Carlo calculation takes input data as screen grid thickness, acceleration grid thickness, screen grid radius, acceleration grid radius, the distance between the grids, and the number of particles to the simulation. Ideal grids are completely transparent, but this is practically not possible. So, the grids must be robust to survive launch and can handle pressure differences.

6.8 Design Configuration - Nominal dimensions and operational parameters of ion optics

- **Total Ion Current**

I_i is the current which is extracted from the plasma:

$$I_i = n_i * e * v_i * A_b \tag{6.51}$$

where: Beamlet area for extracted ions $A_b = \beta_{ext} * As$; and $\beta_{ext} = 0.70$ is area coefficient for ions at the grids.

- **Current Density**

The Child-Langmuir law gives the maximum ion current that an ion accelerator can extract from the discharge chamber to from an accelerated beam for a given applied voltage:

$$J_i = \frac{4}{9}\epsilon_0 . \sqrt{\frac{2e}{m_i}} . \frac{\phi_s^{\frac{3}{2}}}{l_s^2} \tag{6.52}$$

- **Perveance**

It represents the relationship between the maximum current that can be extracted by the grids at a set voltage:

$$P_{max} = \frac{\pi\epsilon_0}{9}\sqrt{\frac{2q}{M}}(\frac{D^2}{d^2})[\frac{A}{V^{\frac{3}{2}}}] \tag{6.53}$$

- **Ion Beam Current**

The ion beam current (I_b) passing through the grid system depends on the effective grid transparency (T_s) and with the area (A_s).

$$I_b = J_i * A_s * T_s \tag{6.54}$$

where: Beamlet area for extracted ions $A_a = \beta_g * A_s$; and $\beta_g = 0.30$ is area coefficient for ions at the grids.

$$I_b = \frac{N_h . (\pi . d_s^2)}{9}\epsilon_0 . \sqrt{\frac{2e}{m_i}} . \frac{\phi_s^{\frac{3}{2}}}{l_s^2} \tag{6.55}$$

- **Grid Transparency**

This ratio is calculated by comparing the total ion beam current with the screen grid current.

$$T_s = \frac{I_b}{I_i} \tag{6.56}$$

which is approximated by this ratio is 0.80%.

- **Beam Voltage**

Here; Vb is the applied potential between the grids is known as beam voltage and the range given is $(1000 - 1500)$ $volts$ with different segmented values.

$$V_b = V_s - V_a \tag{6.57}$$

Higher thrust densities actually occur with more negative accel grid bias because of the higher voltage applied across the screen-to-accel gap for a given net (beam) voltage.

- **Ion exhaust velocity**

The velocity of the propellant exhaust is equivalent to the velocity of the accelerated ions in the beam. Assuming the ions start at rest, the ion velocity leaving the accelerator is:

$$v_i = \sqrt{\frac{2eV_b}{M}} \tag{6.58}$$

where: e_{Vb} is the net beam energy.

- **Propellant mass flow rate**

The ion mass flow rate is related to the beam current. Where M_I is the mass of a single propellant ion:

$$\dot{m}_i = \frac{I_B M_I}{e.B} \tag{6.59}$$

- **Thrust mass utilization efficiency**

η_m is the ratio of propellant flowing out of the thruster that is actually ionized.

$$\eta_m = \alpha_m \frac{I_b M}{e\dot{m}_p} \tag{6.60}$$

where: α_m correction factor for doubly charged ions.

- **Thrust**

Thrust generated is expressed as the flow rate of the propellant multiplied by the velocity of the exhausted propellant from accelerated grids.

$$T = \gamma \dot{m} v_i = \gamma . I_B . \sqrt{\frac{2MV_b}{e}} \tag{6.61}$$

where: $\gamma = \alpha cos\theta$ is a correction factor for double-ion content (α) and θ is the half angle beam divergence. Since the double-ion current is low in RF thrusters and beam half-angle for ion thrusters is 10^0, γ is estimated to be 0.95

- **Specific Impulse**

I_{sp} measures the ratio of thrust to propellant usage, providing a measure of thruster efficiency.

$$I_{sp} = \frac{T}{\dot{m}_p g} = v_i \frac{\dot{m}_i}{g\dot{m}_p} = \frac{\gamma \eta_m}{g} \sqrt{\frac{2eV_b}{M}} \tag{6.62}$$

6.9 Performance

In Ion thrusters, the primary measures of effective conversion of power and propellant to mission change in orbital velocity change ΔV is thrust and specific impulse. An Iodine-fueled inductively coupled Radiofrequency Gridded Ion thruster performance model is implemented Grondein [55] to determine the thrust, Specific Impulse, beam current, and efficiencies.

- **Discharge Efficiency**

The discharge loss per ion is determined by dividing the input power by the ion beam current:

$$\eta_d = \frac{P_{Rf}}{I_b} \tag{6.63}$$

- **Electrical Efficiency**

It relates the actual power of the ion beam P_{beam} to the power P_{Rf} needed in the plasma for extraction of the ion beam current.

$$\eta_{el} = \frac{P_{beam}}{P_{beam} + P_{Rf}} = \frac{I_{beam} * V_b}{I_{beam} * V_b + P_{Rf}} \tag{6.64}$$

- **Thruster Efficiency**

It is calculated by combination of the mass efficiency and electrical. efficiency.

$$\eta_{th} = \eta_m * \eta_{el} \tag{6.65}$$

- **Power Transfer Efficiency**

It is the ratio of power required for ionization to the total RF power:

$$\xi = \frac{P_d}{P_{Rf}} \tag{6.66}$$

6.9.1 RF Thruster Performance Model Parameters

Table 6.8: Thruster model parameters

Parameter	Value	Parameter	Value
Thruster radius, R	50mm	Grid transparency,	0.80
Thruster length, L	30 mm	Mass ow rate, m0	$2.1 * 10^{18}\ m^{-3}$
Chamber volume, V	$9.75 * 10^{-04}$	Particle flow rate, Q0	$1\ mg/sec$
RF coil radius, R_c	3 mm	Molecular mass, M	$127\ a.m.u$
No. of coils, N	5	Grid voltage, V_{grid}	$1250\ volts$
Grid separation, d	0.60 mm	Coil resistance, R_{coil}	$0.317\ m\Omega$
Ion Beam current, I_b	540 mA	Coil applied voltage V_{coil}	$13.68\ Volts$
Radio Freq current, I_{rf}	1.24 A	...	...

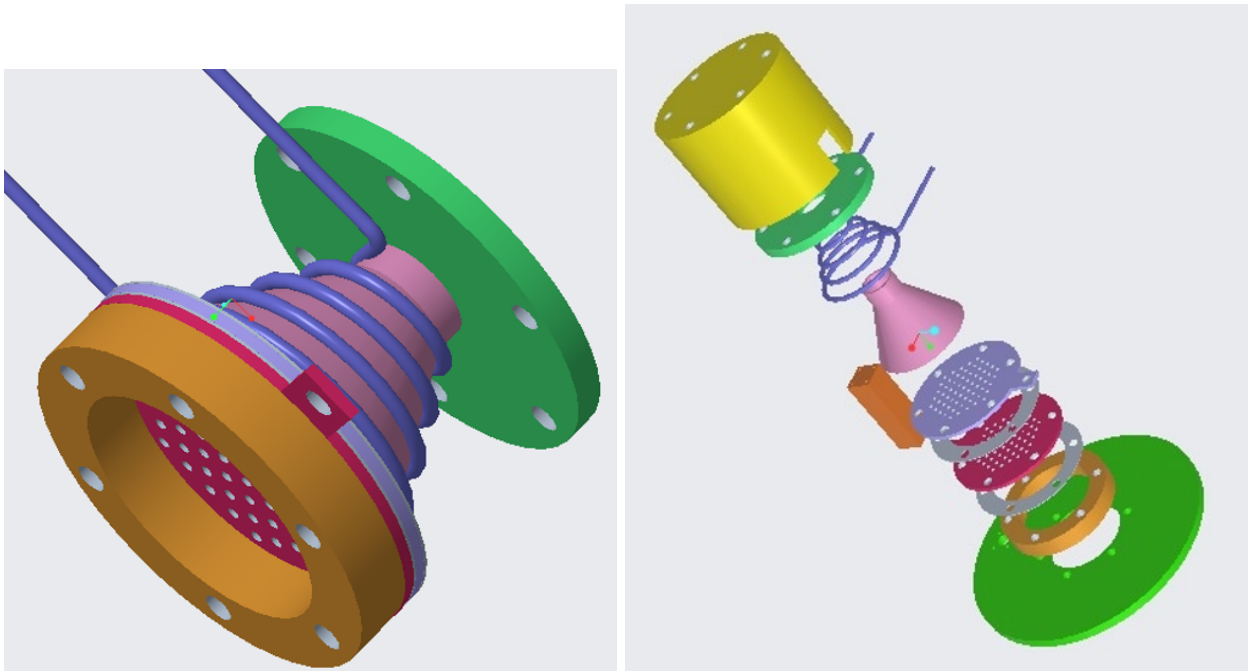

Figure 6.12: Schematic of the electric propulsion system

6.9.2 RF thruster performance at maximum power (39 W)- Electron temperature (2.5 eV)

As the input power increases the power absorbed by plasma increases. This means an increase in ion flux and thrust. The mass utilization efficiency increases but consequently the thrust power efficiency decreases with increases in the power. The thruster performance values are given in the table :

Table 6.9: Performance Parameters (Plasma set with the electron temperature Te = 2.5 eV)

Parameter	Value	Parameter	Value
Max Thrust, T_{max}	28 mN	Mass utilization efficiency, η_m	72.32
Max I_{sp}	3916 sec^{-1}	Discharge Efficiency η_d	70.44
Max Beam Current, I_{beam}	540 mA	Electrical Efficiency η_{el}	94.66
Applied Potential,V_N	1250 volts	Thruster Efficiency η_{th}	66.69

The schematic of the propulsion system is illustrated in Figure 7. The overall design parameters of the electrical propulsion system is summarized in Table 7.

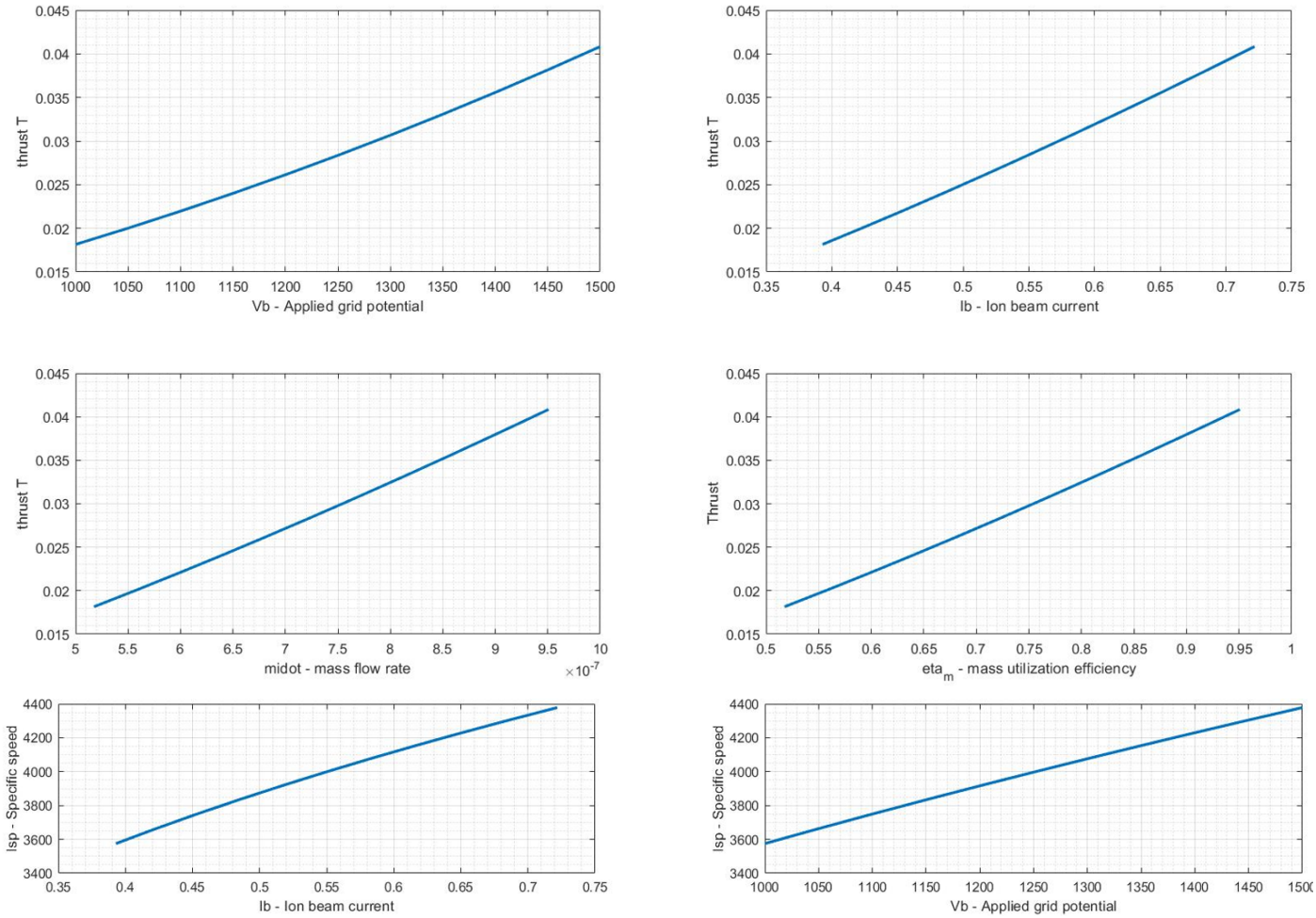

Figure 6.13: Thrust, Isp vs applied potential, Ion beam current and parameters

Table 6.10: Electric propulsion design parameters

Parameter	Value	Parameter	Value
Propellant mass, *mp*	1.16 kg	Feed system Mass,	−−
PPCU Mass,	−−	Thruster mass, mT	−−
Tank volume	$2.31 * 10^{-}04$	Tank radius	3.25 cm
Tank (cylindrical shape)	−−	Tank height	7 cm

With these design parameters and predictions elaborated in the tables, the performance of CubeSats could be theoretically calculated. The most important thing is to understand that the following calculations are only simulated by simulation software's and the actual performance conducted will deviate from the calculations when testing in a real-life experiment.

6.10 Neutralization

Neutralization phenomenon for ion thruster is so important to develop thruster with higher frequency and durability. The main work of the neutralizer is to provide space charge and neutralization current of the ion beam. The neutralizer current can be controlled by adjusting the neutralizer operating envelope (neutralizer voltage) and the associated flow margin of the propellant. It is necessary to determine the optimum flow rate for neutralizer operation. There are different choices for the neutralization process as RF neutralizer, hot cathode, hollow cathode, miniature hollow cathode, and Radiofrequency plasma bridge neutralizer. Due to the challenges regarding design and suitability Miniature hollow cathode is a better option for this thruster assembly. It is a small robust cathode that is designed for low flow rate and low discharge current options. It will produce discharge current of plasma efficiently with propellant flow rates below 1 SCCM, operating at less than 1A current.

The neutralizer as a thruster ignitor With RF ion plasma thrusters, RF systems need free electrons to begin the ionization of neutral propellant flowing in the discharge chamber. So, we need 'seed' electrons in the RF chamber. Field emission occurs when electrons are released from discharge chamber materials induced by the applied electrostatic field. So, the commonly accepted methods use an external neutralizer cathode to provide seed electrons [69]. RF ionization starts vibrating and collides with high energy into neutral gas atoms remaining one electron from it and ionizing the propellant gas. By utilizing the positive screen grid voltage while the acceleration grid is turned off and electrons from the neutralizer enter the discharge chamber while starting the RF unit. After initializing the plasma, the acceleration grid can be turned on and the thruster will start trusting [01,70].

6.11 Radiation Shielding

System design requires the knowledge of the environment in which a satellite must operate to ensure proper operation. Every satellite which is to be operated in space requires protection against higher energy cosmic radiation. LEO ionosphere and GEO sub storm plasma interact differently with the spacecraft. Radiation can be reduced by an absorber placed along the radiation path typical configuration of a silicon device surrounded by an 'Al' absorber under isotropic irradiation.

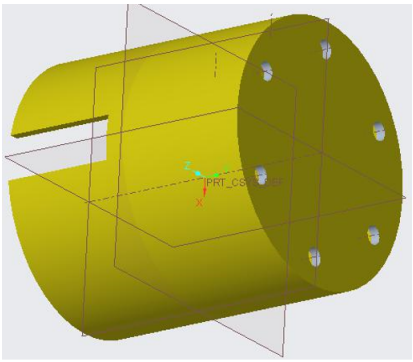

Figure 6.14: Shielding body of thruster

The radiation in LEO is not as harmful as in higher orbits. An aluminum shield should be at least 3 mm thick to effectively block the radiation. But in higher altitude orbits radiation zones are higher therefore, graded shields for a smart solution as Al outside to absorb low energy electrons with no bremsstrahlung and in the back high Z material, absorbing/backstreaming the high energy electrons arrived, till the last thin layer to absorb residual Bremsstrahlung.

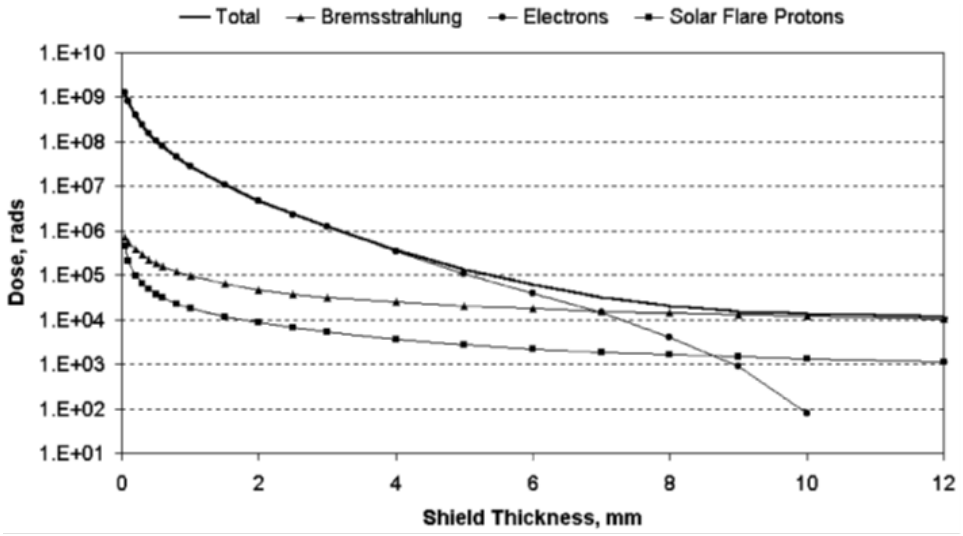

Figure 6.15: TID vs Shield thickness in GEO (20 years)

6.12 Control Systems

Thruster controlling is the most important part of satellite navigation so some control systems must be implemented in our satellites for managing the propellant supply and power distribution. This design does not cover the complete building design of these units but the general functions which are already explained in this research should perform.

6.12.1 Propellant Management

The propellant management system (PMS) is used to supply the iodine in the discharge chamber with the controlled flow. For this, a feeding system model is developed with design software and simulated. Since the system functionality depends on the sublimator and throttles temperatures, this model is equipped with PID temperature controllers, heaters, and temperature sensors. This iodine feeding system architecture is presented in chapter 05.

6.12.2 Power Processing Unit

Power Processing Unit is responsible for the distribution of power to the different systems and subsystems to the satellite. The PPU system is developed here:

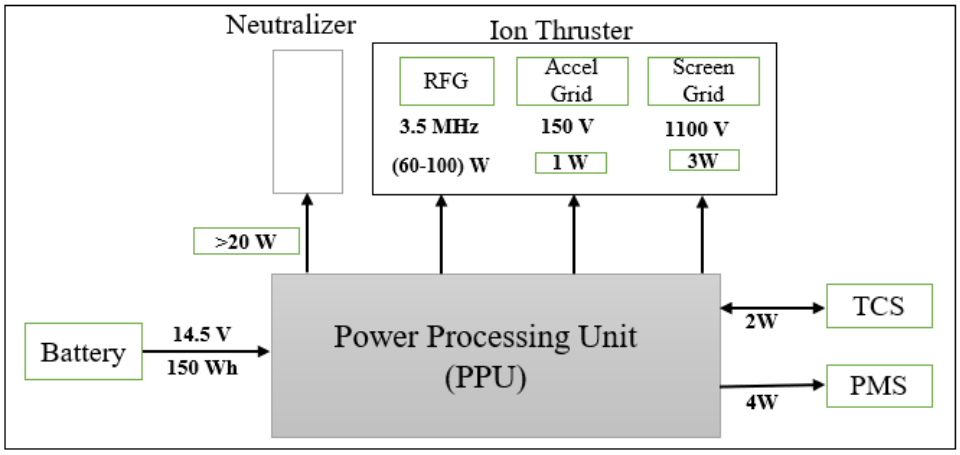

Figure 6.16: Power Processing Unit ow chart.

6.13 Design Solutions Summary

The power budget is made based on a worst-case scenario. The power for the neutralizer is assumed not to exceed 20 watts. The power levels for the PPU, TCS, and PMS is predicted based on the study of similar satellites' power budget. According to the battery pack data sheet, the battery has a thermal control that consumes 6 watts.

6.14 Satellite Characterstics

Taking into consideration that 1U has a mass of 1.33 kg so for 6U CubeSat satellite weight will be 8 kg but with other accessories, the maximum mass will be 6 kg approximately. So, this budget was made to assure that satellite does not exceed the maximum mass for a CubeSat of the size. The parts designed is done in Solidworks, the mass is approximated:

6.14.1 Mass Budget

Taking assumptions regarding the mass of the service module part of the 6U CubeSat to be 1.33kg each. So the maximum allowable mass will be approximately 12 kg. Here, the table shown gives an estimated mass. Since the cable and neutralizer masses are unknown.

Table 6.11: CubeSat design parameters with the thruster

Parts	**Mass (kg)**
Battery,	700 grams
Cables,	200 grams
Fastening	200 grams
Neutralizer	200 grams
Propellant	1000 grams
Feed System	300 grams
Power supply	200 grams
Solar Panels	200 grams
Thruster	300 grams
Thruster Control System	200 grams
Total mass	**3.5 kgrams**

6.14.2 Power Budget

The power budget for the 6U Cubesat satellite-enabled with a Gridded Ion thruster for propulsion. This budget is based on worst-case assumptions. The neutralizer is assumed to not exceed 20 watts and the power levels for PPU, TCS, and PMS are predicted based on the study of power budgets for similar satellites.

Table 6.12: Thruster power budget

System	**Power**
Grids,	(3-8) W
Neutralizer,	$>$ 20W
Propellant Management System	5W
Power Processing Unit	150 Wh
RF Power	(60-100) W

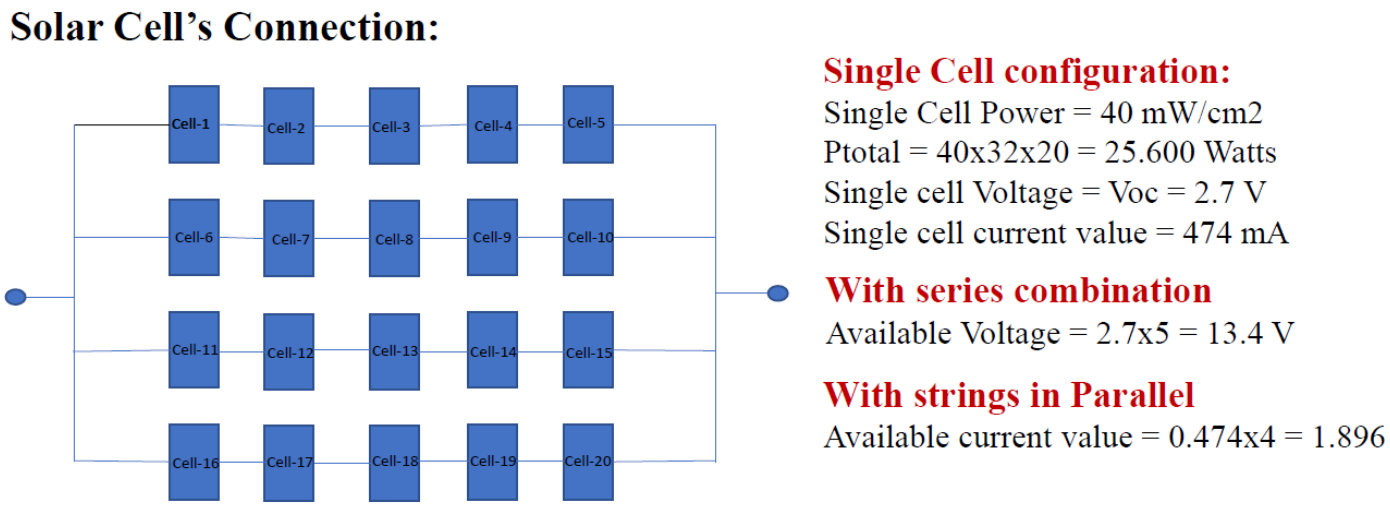

Figure 6.17: Solar Panel

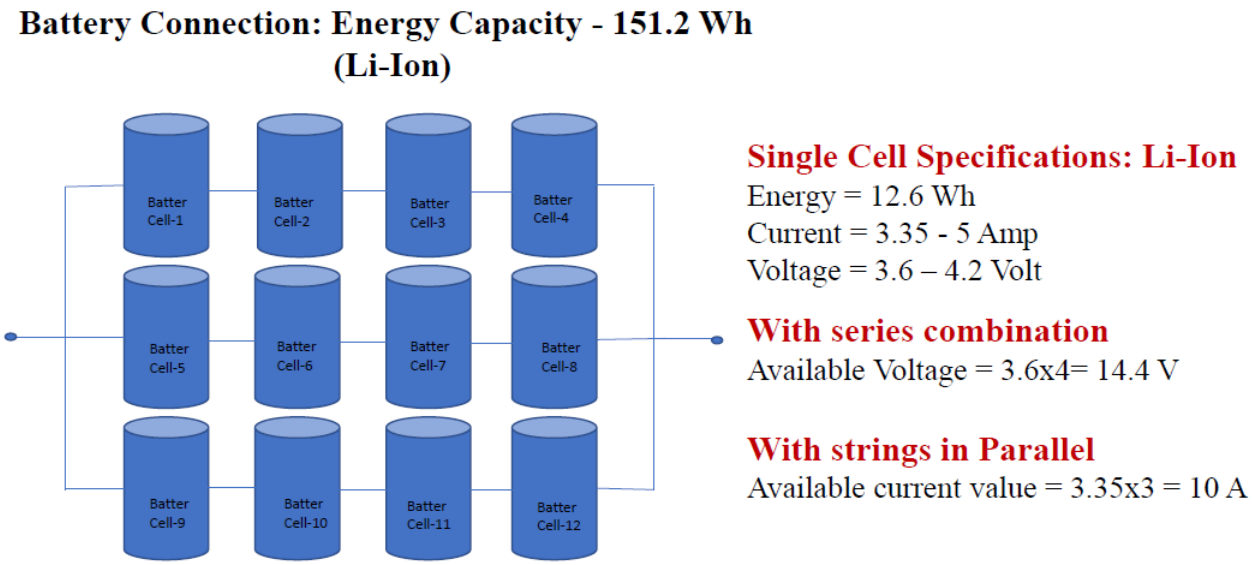

Figure 6.18: Battery System

6.15 Mission Analysis

Placing a satellite into orbit, large rockets and a huge amount of fuel are required. After that, they must be propelled to reach their desired altitude by means of circularization with the optimum trajectory. By considering the orbit rising phase, higher specific impulses imply lower fuel consumption. Therefore, a final orbit with the same departure point can be achieved electrically by spacecraft, which would require less mass than other chemical engines.

6.15.1 Transfer analysis

An orbit around the earth can be either circular or elliptical. Since satellites can not be directly placed into their final orbits. When we used low thrust engines (Electric Propulsion), then the transfer orbit is usually super synchronous (SSTO). An SSTO is either an orbit with a period greater than, that of a synchronous orbit or just an orbit whose apogee is higher than that of a synchronous orbit. Thus way the vehicle raises the perigee and lowers the apogee each turn around the earth. Another low-thrust maneuver using electric propulsion is called spiral climb. It consists of a spiral trajectory around the earth. This is achieved by thrusting continuously in the direction of spacecraft velocity tangentially to the orbit.

Spiral Climb transfer For spiral climb, starting point is low earth orbit (LEO) at 300 km altitude. Thrust is always applied parallel to the velocity vector $\vec{v}$.

$$\vec{a_T} = \frac{T_T}{m} . \frac{\vec{v}}{|v|} \tag{6.67}$$

The initial condition is same as a chemical propulsion. satellite starts at LEO. thus,

$$r_x(t=0) = r1 = 6678km, v_x(t=0) = 0 \tag{6.68}$$

$$r_y(t=0) = 0, v_y(t=0) = v_{c1} = 7.743km/s \tag{6.69}$$

As additional information, required Δv for manoeuvre is directly the difference between the

initial orbit and final orbit velocities. Engines are continuously thrusting over the spiral way.

$$\Delta v_e = v_{c_1} - v_{c_2} = 7.35 - 3.086 = 4.2654 km/sec \tag{6.70}$$

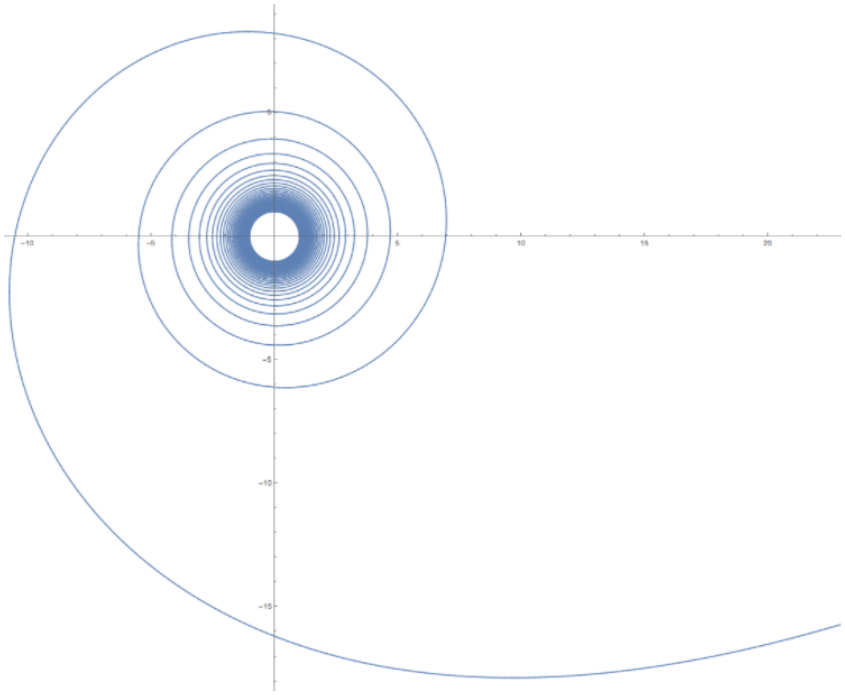

Figure 6.19: spiral from a circular orbit to escape (C3=0)

The Outward Ward Spiral Let us now investigate the transfer of a point satellite of constant mass m from a circular orbit of radius r1 and velocity

$$v_1 = \sqrt{\frac{\mu}{r1}} \tag{6.71}$$

to a higher circular orbit of radius r2 and velocity

$$v_2 = \sqrt{\frac{\mu}{r2}} \tag{6.72}$$

Available is an onboard jet engine that delivers a constant thrust D. Then the satellite will move along a Ward spiral (Figure 6.16)

$$r = \frac{r1}{(1 - (\frac{D}{m})\sqrt{\frac{\mu}{r1}}.t)^2} \tag{6.73}$$

until it reaches the new orbit radius $r2$ at time tw

$$r2 = (\frac{r1}{(1 - (\frac{D}{m})\sqrt{\frac{\mu}{r1}}.tw)^2} \tag{6.74}$$

At that moment, the engine is turned off, causing $\dot{r} = 0$ from equation and the satellite now moves on a new circular orbit. From equation (6.64), the time to traverse the Ward spiral orbit is

$$tw = \frac{m}{D}\frac{\mu}{r1}(\sqrt{\frac{r1}{r2}}) = \frac{m}{D}(v1 - v2) \tag{6.75}$$

The angle swept out during Ward transfer, from equations is

$$\theta_w = \frac{m}{D}\frac{\mu}{r_1^2}(1 - \sqrt{\frac{r1}{r2}}) \tag{6.76}$$

we select a thrust of $D = 5mN$. The transfer spiral is then

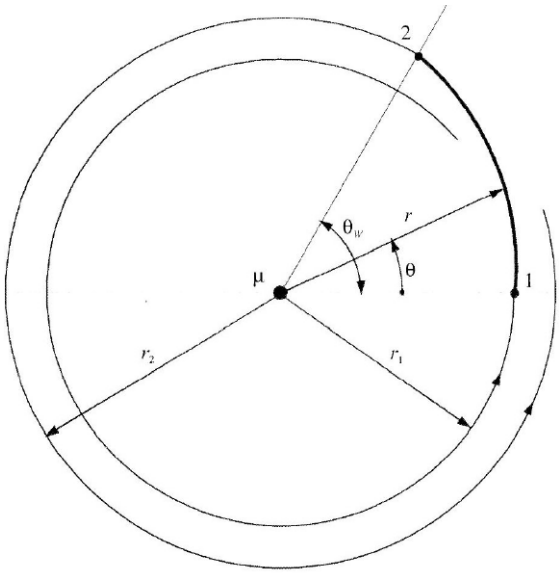

Figure 6.20: Ward Transfer between Points 1 and 2

The velocity change rate is

$$\dot{v} = \frac{D}{m} \tag{6.77}$$

giving a velocity change during the transfer of

$$\Delta v = \dot{v} * tw \tag{6.78}$$

as it is required. It represents the difference between the two orbital velocities

$$v_1 = 7.31 km/sec \tag{6.79}$$

$$v_2 = 3.08 km/sec \tag{6.80}$$

The transfer between circular orbits by means of the Ward spiral has been described for a transfer from a circular base orbit to a higher target orbit which dependent on the thrust.

Chapter 7

Conclusions

By doing qualitative analysis, Iodine proved as a feasible alternative to xenon because of its good propulsive performance and possible to be stored in a solid-state at ambient temperature and lower pressure, while xenon is rare, expensive to produce, and requires higher storage pressure. As this work was to design a robust Gridded ion thruster using the discharge plasma generation technique, the proposed shape of the discharge chamber as conical prevented excessive loss of ions to the walls. Secondly, For grid design, an evolutionary algorithm with the ffx ion optics presented by 'Farnell' was used to optimize the grid geometry and accelerator grid voltage to set with regard to maximizing impulse per unit area. Grid operating condition, including a net accelerating voltage of 1250 volts and Ion beam current is 540 mA. Lastly, This model is assumed valid for most reasonable regimes of thruster operations. The prediction of the model was verified by experimentally obtained performance mapping. WE found that the thruster would be 28 mN specific impulse of 3997 m/s,for 1250 Watt of RF power. In these conditions, the mass utilization efficiencies are about 72.32 %, electrical efficiency is 94.66 % and overall thruster efficiency is 66.69 %. Thus, Such a propulsion system will provide (3.0-4.0) km/sec of delta-V capability for a 6U/12 kg spacecraft, which will enable a variety of missions Lunar cube, inner planet flyby, asteroid rendezvous.

Future Work We will continue to conduct experimental tests to verify local plasma parameters in the discharge chamber with an arbitrary shape and to improve simulation accuracy. Additionally, the built feed system will be tested to determine the thermal capability of producing and controlling plasma. Also, we will test the built feed system's thermal capability of producing and controlling iodine mass flow rates with reduced power requirements and good throttling. We can also test it experimentally and put it into production.We can also test the system experimentally and put it into production.

Appendix A

Appendix

A.1 Appendix A - Calculation for Matching Network Parameters

Calculations with this appendix is based on one assumption that the resistance of the RF generator is 50 Ω.

The conical coil can be calculated by Harold Wheeler formulas, which Tesla was using.

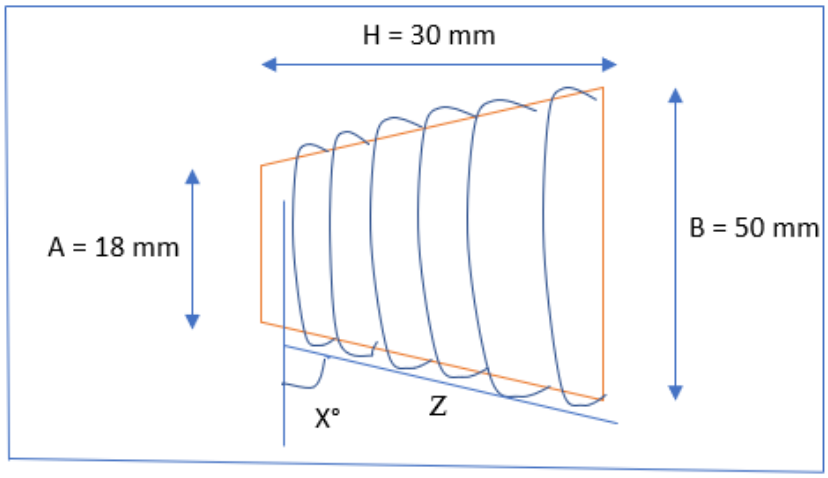

Figure A.1: The outer dimensions of discharge chamber

$N = 5$ - number of turns
$A = 18$ mm - diameter of base of cone
$B = 50$ mm - diameter of top of cone
$H = 30$ mm - height of cone
$W = \frac{B-A}{2} = 16$ mm - effective width of coil
$Z = \sqrt{W^2 + H^2} = 34$ mm - length of coil (along hypotenuse)
X $= 29°$ $(sin(X) = H/Z; cos(X) = W/Z)$ - cone angle
R $= \frac{A}{2} + \frac{W}{2} = 17$ mm - Average radius of the chamber

Now, The vertical component of inductance L1 and horizontal component L2 could be calculated by these formulas:

$$L_1 = \frac{R^2 N^2}{9R + 10H} \tag{A.1}$$

$$L_2 = \frac{R^2 N^2}{8R + 11H} \tag{A.2}$$

The total inductance of the coil is obtained by [].

$$L = \sqrt{(L_1 sinx)^2 + L_2 cosx)^2} \tag{A.3}$$

The units of calculated inductance is in μH. By solving this equation , the value of L = 0.5 μH

The coil impedance $Z_L = R_L + j\omega L$. The internal coil resistance R_L for copper wire is very less 45 $m\Omega$ so therefore, it is neglected. The coil impedance is therefore $Z_L \approx j\omega L$

$$Z_L = j\Omega L = j \times 2\pi \times 3.5 MH_z \times 0.5 \mu H = 11 j\Omega \tag{A.4}$$

Since the impedance of the coil does not match the impedance of the the RF generator, a matching network is required.

And this is done by parallel coupling of a capacitor with the size which is provides resonance to the antenna coil.

The capacitance which gives the resonance if calculated by.

$$C_1 = \frac{1}{2\pi f X_{C_1}} = \frac{1}{2\pi \times 3.5 MH_z \times 11\Omega} = 4.13 nf \tag{A.5}$$

To match the source impedance of 50 Ω, a capacitor will be placed in series with the source.

The capacitance of C_2 is

$$C_2 = \frac{1}{2\pi f X_{C_2}} = \frac{1}{2\pi \times 3.5 MH_z \times 50\Omega} = 1.0 nf \tag{A.6}$$

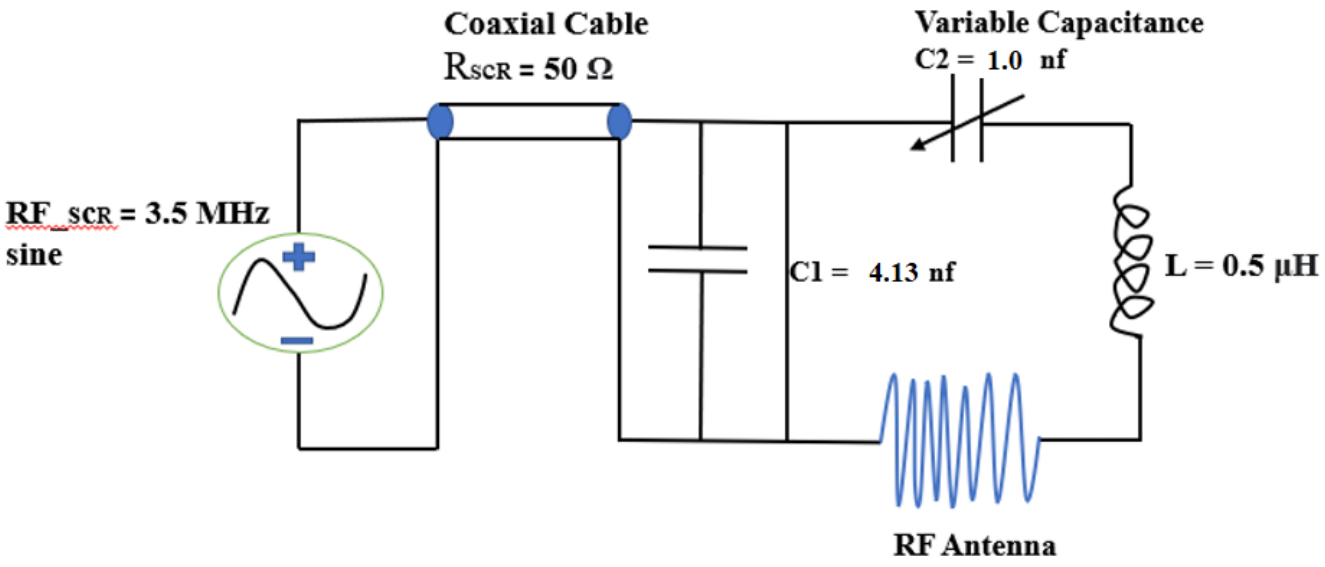

Figure A.2: Circuit diagram: Matching Network

A.2 Appendix B - Calculations of propellant mass and operation time

For Interplanetary missions, If required Δ V = 4 km/sec then the value of mass propellant required with a specific impulse of $I_{sp} = 3997\ sec^{-1}$ can be calculated with the help of Tsiolkovsky's Equation:

$$\Delta v = v_e * ln(\frac{mi}{mf}) = g * I_{sp} * ln(\frac{mi}{mf}) \tag{A.7}$$

By simplifying:

$$m_p = m_i * (1 - exp(-\frac{\Delta_V}{V_e})); \tag{A.8}$$

with these values the approximated weight of the Iodine is 1160 $Grams$ or 1.16 kg. With this weight of Iodine Its possible to calculated the dimensions of the tank: Volume of cylinder

$$V = \pi r^2 h \tag{A.9}$$

Estimated mass of the propellant m_p = 1.1638 $kgrams$ Number of moles x atomic weight = 1075 $grams$ To obtain a pressure of 1 bar at room temperature (27^0C or 300^0k)inside the tank, number of moles can be found by utilizing the ideal gas equation:

$$\eta = \frac{V * P}{R * T} \tag{A.10}$$

No. of moles

$$\frac{wt}{atomicwt} = \frac{1072}{127} = 8.44moles \tag{A.11}$$

For Iodine unit SCCM is equal to the $4.4779 * 10^{17}$ atoms per second when discussing Iodine flow rates, which in the case of the chosen flow rate of $1mg/sec = 10\ SCCM$ means $4.4779 * 10^{18}$ atoms per second. Dividing the total number of atoms by this value gives the number of constant thruster operation seconds $\frac{5.08*10^{24}}{4.4779*10^{18}} = 1135262$ seconds.

As estimated, the thruster can operate in 1 hour before the battery require charging ($1hour = 3600seconds$). To find the number cycles, the seconds of the constant thruster operation is divided by the number of seconds in 1 hour. Number of cycles = $\frac{1135262}{3600} = 316$

Table: Weight of Iodine required and the Tank size:

System Specifications		
Launch Mass (6U Cubesat),	m_i	12 kg,
Density of Iodine (I)	ρ_I,	4930 kg/m^3
Propellant weight (I)	m_p	1.16 kg
Change of orbital velocity	ΔV	4 km/sec
Tank Specifications		
Diam of the tank	D_{tank}	6 cm
Height of the tank	h	8 cm

Acknowledgements

In the present world of competition, there is a race of existence in which those are having strong willpower come forward to success. This work is like a bridge between theoretical and practical work, with this willing I started this particular work.

It is, therefore, my honor to express my deepest thanks to those who have made this thesis possible. I owe my wholehearted gratitude to my supervisor, **Prof. Antonella Ingenito** whose guidance and support enabled me to carry on with this work. Her expertise and opinions have been instrumental in the completion of my thesis. I am very thankful to **Prof. Parisse Maurizio** who taught me the initial basics of the Design of Space Systems.

I would like to give special thanks to my father - **Gulfam Ali** and my mother - **Shahjahan Begum** as a whole for their continuous support, your prayers for me were sustained me this far.

I also would like to thank **'School Aerospace Engineering'**,'Sapienza University of Rome'', Italy to provide such a unique platform to gain knowledge. Here, all the professors are the gem of knowledge and have an amazing way of teaching. Finally, I would like to thank **Prof. Paolo Toeffilato** and **Prof. Giovanni Palmerini** two strong pillars of this walled, esteemed prestigious research center, Roma, Italy.

Navaid Ali,
Rome, Italy
Jan - 2022

Bibliography

[1] D. Goebel and I. Katz. Fundamentals of electric propulsion. john wiley sons. *John Wiley Sons, Hoboken, NJ*, 2008.

[2] G. Aston and P. J. Wilbur. Ion extraction from a plasma. *J. Appl. Phys.*, 52(4):2614–2626, 1981.

[3] W.Andrew Hoskins. 30 years of electric propulsion flight experience at aerojet rocketdyne. October 2013.

[4] An ion propulsion farther, faster, cheaper. *Nasa.Gov*, August 2017.

[5] Lee.S Hutputanasin.A Toorian.A Lan.W and 'Munakata.R. Cubesat design specification,san luis obispo. 2009.

[6] E. Y. Choueiri. A critical history of electric propulsion: the first 50 years (1906-1956). *Journal of Propulsion and Power*, 20(2):193–203, 2004.

[7] R. H. Goddard. The green notebooks. *The Dr.Robert H. Goddard Collection at the Clark University Archives, Clark University, Worchester, Massachusetts.*

[8] T. M. Mel'kumov. Pioneers of rocket technology, selected works, inst. for the history of natural science and technology. *translated from the 1964 Russian text by NASA as NASA TT F-9285*, 1964.

[9] R.G.Jahn. Physics of electric propulsion. *Journal of Applied Physics*, 1968.

[10] R. J. Cybulski D. M. Shell hammer R. R. Lovel E. J. Domino and J. T. Kotnik. Results from sert i ion rocket flight test. *National Aeronautics and Space Administration, Washington*, 1965.

[11] A. S. Kim V. P. Popov G. A. Bober. State of the works of electrical thrusters in the ussr. *In 22nd International Electric Propulsion Conference, Viareggio, Italy.*, 1991.

[12] J. R. Brophy. Nasa's deep space 1 ion engine. *Review Scientific Instruments*, 73(2):1071–1078, 2002.

[13] H. Kuninaka. Ambitious challenges of japanese electric propulsion. *In 29th International Electric Propulsion Conference, Princeton, NJ*, 2005.

[14] C. R. Koppel and D. Estublier. The smart-1 hall effect thruster around the moon: in flight experience. *In 29th International Electric Propulsion Conference, Princeton, NJ.*, 2005.

[15] Killinger R. Leiter H. and Kukies R. Rita ion propulsion systems for commercial and scientific applications. *In 43rd AIAA/ASME/SAE/ASEE Joint Propulsion Conference Exhibit, Cincinnati, OH.*, 2007.

[16] Garner E. C. Rayman M. and Brophy J. R. In-ight operation of the dawn ion propulsion system through year one of cruise to ceres. *In 49th AIAA/AS-ME/SAE/ASEE Joint Propulsion Conference, San Jose, CA.*, 2013.

[17] Snyder J. S. Goebel D. M. Hofer R. R. Performance evaluation of the t6 ion engine. *Journal of Propulsion and Power*, 28(2):371–379, 2012.

[18] J. R. Brophy and B. Muirhead. Near-earth asteroid retrieval mission (arm) study. *In 33rd International Electric Propulsion Conference, Washington, DC*, 2013.

[19] S. N. Williams and V. C. Carroll. Mars missions using solar electric propulsion. *Journal of Spacecraft and Rockets*, 37(1):71–77, 2000.

[20] Loeb H. W. Freisinger J. Groh K. H. State-of-the-art of the rit ion thrusters and their spin-o$_s$. *In 39th Congress of the International Astronautical Federation, Bangalore, India.*, 1988.

[21] G. Fortescue P. W. Swinerd and Stark J. Spacecraft systems engineering. *John Wiley Sons, Chichester, 4th edition*, 2011.

[22] G P Sutton and Biblarz. Rocket propulsion elements. *John Wiley Sons, Hoboken, N.J, 8th editio*, 2010.

[23] C Turner J Puig-Suari and W Ahlgren. Development of the standard cubesat deployer and a cubesat picosatellite. *IEEE Aerosp Conf Proc*, 2001.

[24] Kurt Hohman Michael Tsay, John Frongillo. Lunar cube: A deep space 6u cubesat with mission enabling ion propulsion technology. *Paper SSC15-XI-1, 29th AIAA/USU Conference on Small Satellites North Logan, Utah*, pages 8–13, August 2015.

[25] Alexander L MAJ Jehle. Iodine small satellite propulsion demonstration–isat'. *NASA, MSFC Technology Development Transfer Office –ZP30 U.S. Army Space and Missile Defense Command/Army Strategic Command.*

[26] J.Mueller R.Hofer M.Parker and J.Ziemer. Survey of propulsion options for cubesats. *57th JANNAF Propuls. Meet*, pages 1–56, 2010.

[27] Mats Fredrik Heigre Varin Sund Hogne Andersen. Design proposal of tigris - a cubesat ion propulsion system. *https://www.researchgate.net/publication/304495110*, May 2016.

[28] J. M. Lafferty. Boride cathodes. *Journal of Applied Physics*, 22(1):299, 1951.

[29] K.H.Groh O.Blum H.Rado and H.W.Loeb. Inert gas radiofrequency thruster rit 10. *presented at the 14th Int. Electric Propulsion Conf., Princeton, NJ, IEPC-79-2100*, May 1979.

[30] H. Goede W.F.Divergilio and V. V. Fosnight. High frequency plasma generators for ion thrusters,nasa, washington, dc, nov. 1981, nasa cr-167957. Nov 1981.

[31] Hohman K Tsay M and Olson L. Micro rf ion engine for small satellite applications.

[32] Busek RF Ion Thrusters (Datasheet). Busek space propulsion and system.

[33] Carlos Sánchez Lara. Design and performance analysis study of an ion thruster' polytechnic university of catalonia (upc).

[34] H. R. Kaufman. Technology of closed-drift thrusters. *AIAA Journal*, 23(1):78–87, 1985.

[35] J.R.Beattie P.J.Wilbur and J.Hyman Jr. An approach to the parametric design of ion thrusters," in spacecraft propulsion and power. page 467–475, 1988.

[36] J.D.Williams R.A.Martinez and D. M. Goebel. Electric field breakdown properties of materials used in ion optics systems. *AIAA-2006-5004*, July 2006.

[37] P. J. Wilbur and V. K. Rawlin. Ion thruster development trends and status in the united states introduction. *J. Propuls. Power*, 14:5, 1998.

[38] H.Kuninaka I.Funaki K.Nishiyama Y.Shimizu and K.Toki. Results of endurance test of microwave discharge ion thruster engineering model. *AIAA-2000-3276*, pages 16–19, july 2000.

[39] Bechtel R.T. A hollow cathode neutralizer for a 30-cm diameter bombardment thruster. 1973.

[40] J.S.Sovey J.A.Dever and J.L.Power. Retention of sputtered molybdenum on ion engine discharge chamber surfaces. *IEPC-01-86*, pages 15–19, October 2001.

[41] D. M. Goebel and A. C. Schneider. High voltage breakdown and conditioning of carbon and molybdenum electrodes. *IEEE Transactions on Plasma Science*, 33:1136–1148, October 2005.

[42] Lieberman M.A.and Lichtenberg A.J. Principles of plasma discharges and materials processing.

[43] F.F.Chen. Introduction to plasma physics and controlled fusion volume 1:plasma physics. 1984.

[44] W.F.Divergilio H.Goede and V.V.Fosnight. High frequency plasma generators for ion thrusters, nasa, washington, dc,. Nov 1981.

[45] Mistoco V. Modeling of small-scale radio-frequency inductive discharges for electric propulsion application. 2011.

[46] A.D.MacDonald. Microwave breakdown in gases. new york, wile. 1966.

[47] J.R.Brophy D.E.Brinza J.Polk M.Henry and A.Sengupta. The ds1 hyper-extended mission,38th joint propulsion conf., indianapolis, in. July 2002.

[48] P.Chabert J.Arancibia Monreal J.Bredin L.Popelier and A.Aanesland. Global model of a gridded-ion thruster powered by a radiofrequency inductive coil. *Phys. Plasmas*, 19, 2012.

[49] P.Chabert and N.Braithwaite. Radio-frequency plasmas. *Cambridge University Press, Cambridge*, 2011.